ADVANCED ELECTRONIC MATERIALS
Open Access
www.advelectronicmat.de

Million-Atom Simulation of the Set Process in Phase Change Memories at the Real Device Scale

*Omar Abou El Kheir and Marco Bernasconi**

Phase change materials are exploited in several enabling technologies such as storage class memories, neuromorphic devices and memories embedded in microcontrollers. A key functional property for these applications is the fast crystal nucleation and growth in the supercool liquid phase. Over the last decade, atomistic simulations based on density functional theory (DFT) have provided crucial insights on the early stage of this process. These simulations are, however, restricted to a few hundred atoms for at most a few ns. More recently, the scope of the DFT simulations is greatly extended by leveraging on machine learning techniques. In this study, it is showed that the exploitation of a recently devised neural network potential for the prototypical phase change compound $Ge_2Sb_2Te_5$, allows simulating the crystallization process in a multimillion atom model at the length and time scales of the real memory devices. The simulations provide a vivid atomistic picture of the subtle interplay between crystal nucleation and crystal growth from the crystal/amorphous rim. Moreover, the simulations have allowed quantifying the distribution of point defects that controls electronic transport, in a very large crystallite grown at the real conditions of the set process of the device.

1. Introduction

Chalcogenide glasses, such as the prototypical $Ge_2Sb_2Te_5$ (GST) compound, are exploited in non-volatile electronic memories, either standalone[1–3] or embedded in microcontrollers,[4,5] and in devices for in-memory and neuromorphic computing.[6–8]

These applications rely on a fast and reversible transformation between the crystalline and amorphous phases induced by heating.[1] The two phases feature a difference in resistivity by three orders of magnitude that allows encoding a binary information which can be read out by a measurement of resistance at low bias.[1] Amorphization of the crystal via melting (reset) and recrystallization of the amorphous phase (set) are achieved by applying current pulses at higher bias.[1,2] Partial recrystallization during set or modulation of the size of the amorphous region during reset are also possible to obtain intermediate discrete or analogic resistance levels for in-memory and neuromorphic computing.[8]

The crystallization kinetics is thus a key functional property that determines the programming time of the memory and as such it has been the subject of extensive experimental and theoretical studies over the years.[9] Experimental works have shown that GST exhibits a nucleation driven crystallization in which several overcritical crystalline nuclei form and then slowly grow.[10] Other materials in this class, such as AgInSbTe alloys,[10] feature instead a growth driven crystallization which mostly proceeds at the interface between the amorphous inclusion and the crystalline matrix with no or marginal crystal nucleation. This distinction depends, however, on the temperature and on the size of the amorphous region which is ruled by the device architecture. Information on the crystallization kinetics at the device level is obtained indirectly from electrical measurements supplemented by phenomenological modeling of the electrothermal processes (see Refs. [11, 12] for a review). The electrothermal modeling, however, relies on several parameters on the physical properties of the material which are only partially known at the operation conditions of the device. Moreover, classical nucleation theory is typically applied which might be inaccurate for very small critical nuclei (a few tens of atoms) as is the case for GST in the temperature range of the set process.

On the other hand, molecular dynamics (MD) simulations based on DFT provided crucial insights on the early stage of nucleation and growth in models containing a few hundred atoms.[13–20] Most recently, machine learning techniques[21,22] allowed extending the scope of DFT methods by providing interatomic potentials fitted on a DFT database that have enabled large scale simulations of phase change materials.[23–35] In particular, interatomic potentials generated with neural network (NN) methods[21] enabled the simulations of a few thousand atoms for tens of ns that provided information on the crystal growth velocity in a wide range of temperatures for GeTe[24,36] and GST.[32] Very recently, a Gaussian Approximation Potential (GAP)[22] for GST allowed simulating the reset process (crystal melting) in a 532 980-atom model at a length scale close to that of the real memory device.[29] This is, however, the fast process in the memory

O. Abou El Kheir, M. Bernasconi
Department of Materials Science
University of Milano-Bicocca
via R. Cozzi 55, I-20125 Milano, Italy
E-mail: marco.bernasconi@unimib.it

The ORCID identification number(s) for the author(s) of this article can be found under https://doi.org/10.1002/aelm.202500110

DOI: 10.1002/aelm.202500110

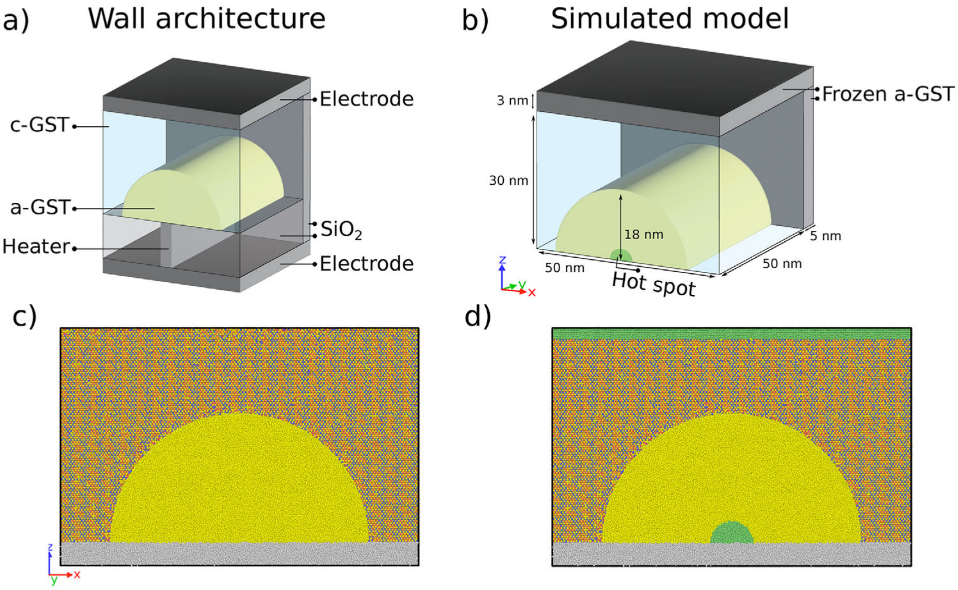

Figure 1. a) Sketch of the active region of a PCM in the Wall architecture.[41] A semi-cylindrical region of a-GST is embedded in a crystalline matrix (c-GST, not shown) and confined by dielectrics (SiO_2) in the y direction and by the top and bottom electrods in the z direction. The heater in contact with a-GST and embedded in SiO_2 is also shown. b) Atomistic model of the PCM cell with 3D periodic boundary conditions. The gray regions correspond to the confining materials (frozen GST, see text), the yellow region is the active amorphous semi-cylindrical dome, embedded in a crystalline matrix (not shown). The smaller semi-cylindrical green region highlights the atoms inside the dome thermostatted at 880 K that mimics the hot spot generated by the heater underneath (see text for simulation C). c) A front view of the model with atomic resolution. d) The same of panel c) with the semi-cylindrical green region corresponding to the hot spot thermostatted at 880 K and the other green region in the upper part of the model that indicates atoms thermostatted at 600 K in simulation B or at 300 K in simulation C (see text). The Ovito.[44] tool was used for the visualization and the generation of all atomic snapshots of this article.

programming that requires MD simulations lasting a few tens of ps.

In this work, we show that it is possible to simulate the slow process in memory operations, i.e., the crystallization of the amorphous phase (set) at the length and time scales of the real memory devices, by exploiting the efficient implementation on graphical processor units (gpus) of the DeePMD code[37–39] that we used previously to generate a NN potential for GST.[32] MD simulations of models with 2.795 million atoms have allowed us to visualize at the atomic level the recrystallization of an amorphous dome embedded in a crystalline matrix on the time scale of a few ns.

2. Results and Discussion

2.1. Modeling of the Phase Change Memory Cell

We modeled the active region of a phase change memory (PCM) device in the Wall architecture[40] sketched in **Figure 1a** which is used for embedded applications.[41] The active material is surrounded by dielectrics, by the top electrode, and by the heater which is a resistor that releases heat via the Joule effect. In the Wall architecture, the increase in temperature in the active material is mostly due to the heat released within the heater. A hot spot is then generated within the GST in contact with the heater. Self-heating through the Joule effect within the transforming material itself is much less important and is typically neglected.[42] In place of the dielectrics and electrodes that confine the GST film, we used a thin film (3 nm thick) of still amorphous GST (a-GST) whose atoms were frozen at zero temperature to mimic the high thermal stability of the materials surrounding the active region. The simulation unit cell with 3D periodic boundary conditions is shown in Figure 1b. The light gray regions correspond to frozen a-GST atoms that mimic the surroundings of the active GST film which consists in turn of a semi-cylindrical amorphous dome embedded (yellow region) in a crystalline matrix (not shown). The radius of the amorphous dome and the thickness of the GST film along the z and y directions shown in Figure 1b have values typical of the Wall architecture for embedded memories.[43] The model contains 2.323 million mobile atoms and 0.472 million atoms in the frozen layers. The semi-cylindrical amorphous dome contains 786 412 atoms. A snapshot of the model with atomic resolution is shown in Figure 1c.

To generate the model of Figure 1b,c, we started from cubic GST at the theoretical density of 0.0309 atom/Å^3.[32] The crystalline cubic matrix was built by replicating the model generated in Ref. [45] with a random distribution of Sb, Ge, and stoichiometric vacancies in the cationic sublattice. The amorphous confining layers and the active amorphous dome were then generated by heating these regions at 1400 K for 20 ps and then quenching to 600 K in 100 ps, while all the other atoms were always thermostatted at 600 K. The amorphous confining layers were then frozen in all the subsequent simulations.

For the simulation of the crystallization, we must consider that thermal conductivity κ allows the latent heat released during the crystallization to diffuse away from the crystal growth front. At the same time, κ is also responsible for the heat transfer from the hot spot at the heater to the bulk of the

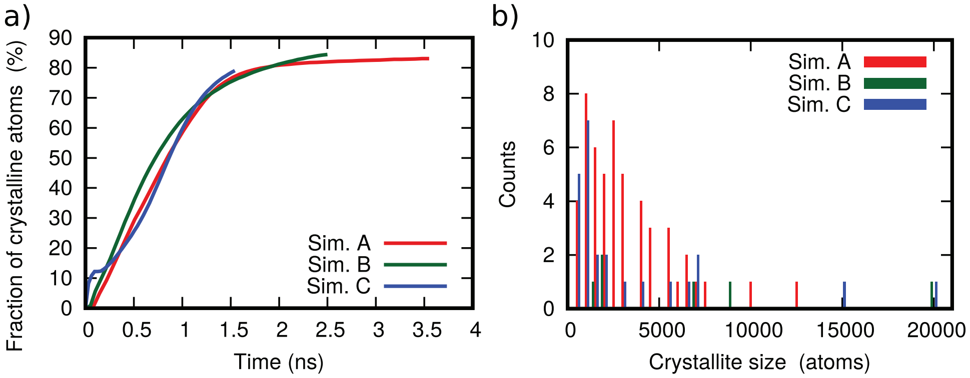

Figure 2. a) Fraction of atoms in the active region that are recrystallized as a function of time in the PCM model of Figure 1b, under different conditions (simulations A/B/C, see text). b) Distribution of the size of crystallites nucleated inside the dome.

transforming material. In the crystalline cubic phase, κ is mainly due to phonons (0.4 W/mK) while electrons contribute about 10 % (0.04 W/mK).[46] In the amorphous phase, κ is due only to phonons. In the supercooled liquid phase at temperatures above the metal-semiconductor transition (M-SC),[47,48] the contribution of electrons to κ is supposed to be higher, although we do not have a reliable estimate for this quantity. DFT simulations estimated the M-SC transition in the temperature range 750–850 K in the supercooled liquid phase.[47] In our simulation, in the lack of the explicit modeling of electrons, the thermal conductivity is sustained only by phonons which is, anyway, a reliable approximation at the temperature conditions of the set process (see below). The crystallization of the amorphous dome was simulated by controlling temperature in three different manners as described below.

First, we performed a simulation by applying two independent thermostats for atoms in the crystalline matrix and in the amorphous region at the same target temperature of 600 K. This protocol (simulation A) allows us to efficiently remove locally the latent heat released during the crystallization. In a second simulation (simulation B), we considered the other extreme in which the latent heat is removed only by the upper electrode. This is mimicked by applying a thermostat at 600 K only to a thin crystalline film 3 nm thick in contact with the frozen layers mimicking the upper electrode, after having equilibrated both the embedding crystal and the embedded amorphous dome at 600 K. In a third and more realistic simulation (simulation C), we applied two thermostats at two different temperatures. One thermostat as above is applied only to a thin crystalline film 1.5 nm thick in contact with the frozen layers mimicking the upper electrode and set to 300 K. The second thermostat is applied to a small semi-cylindrical region with radius 30 Å in the lower part of the dome (see Figure 1d). The second thermostat is set to 880 K to mimic the hot spot generated by the heater underneath, as was shown by finite-elements simulations of the operation of the device in Ref. [49]. Since in this architecture heat is mostly released by the heater, as mentioned above, Joule self-heating within the transforming GST material is neglected in the simulation. Moreover, since the surrounding materials along y and z are frozen, they have an infinite thermal boundary resistance. However, as shown in Ref. [43], in the Wall architecture the main path for heat dissipation is from the hot spot at the heater toward the top electrode where we placed a thermostat to mimic heat dissipation. We then expect that the condition of infinite thermal boundary resistance with the surrounding has a minor effect on the overall behavior of the device.

2.2. Simulation of the Set Process

We first analyze the results of simulation A with the dome thermostatted at 600 K. The evolution in time of the fraction of the recrystallized atoms is shown in **Figure 2**a, while snapshots of the system at different times are shown in **Figure 3**. To identify the crystalline nuclei, we used the local order parameter Q_4^{dot}[50] that we considered in our previous work on the crystallization of bulk GST.[32] Most of the crystallization takes place at the crystal-amorphous rim which moves inwards with time, but crystal nucleation is also present inside the amorphous dome.

The largest crystallite grown from the amorphous-crystal interface contains 541 233 atoms which amount to 88 % of the total number of recrystallized atoms. The distribution of the size of the smaller crystallites nucleated inside the dome is shown in Figure 2b. About 75% of the atoms crystallizes rapidly in the first 1.5 ns, then a slow down takes place due to the interaction among several nuclei, about 55, formed within the dome. The fraction of crystallized atoms then increases very slowly and reaches a plateau around 80% at 3.5 ns. Most of the crystallites nucleated inside the dome contains less than 3000 atoms, but a few grow up to 12.000 atoms (see Figure 2b). These crystallites are expected to undergo a coarsening on a longer time scale. In our previous work[32] on the simulation of homogeneous crystallization of GST at 680 K, it was shown that coarsening of the smaller crystallites occurs on the time scale of 20 ns in a 27 000 atoms cell.

The crystal growth velocity v_g of the crystallite growing from the interface has been computed from the evolution of the radius of the semi-cylindrical dome (R_c) and is given by $v_g = -\,dR_c(t)/dt$, with $R_c = \left(\left(V_{active} - N\rho_{cubic}^{-1}\right)/\pi l_c\right)^{\frac{1}{2}}$ where V_{active} is the volume of the active region, N is the number of crystalline atoms in the crystallite, ρ_{cubic} is the density of cubic phase and l_c is the length of the semi-cylindrical dome. On the other hand, v_g of the crystallites nucleated inside the dome can be estimated by assuming a

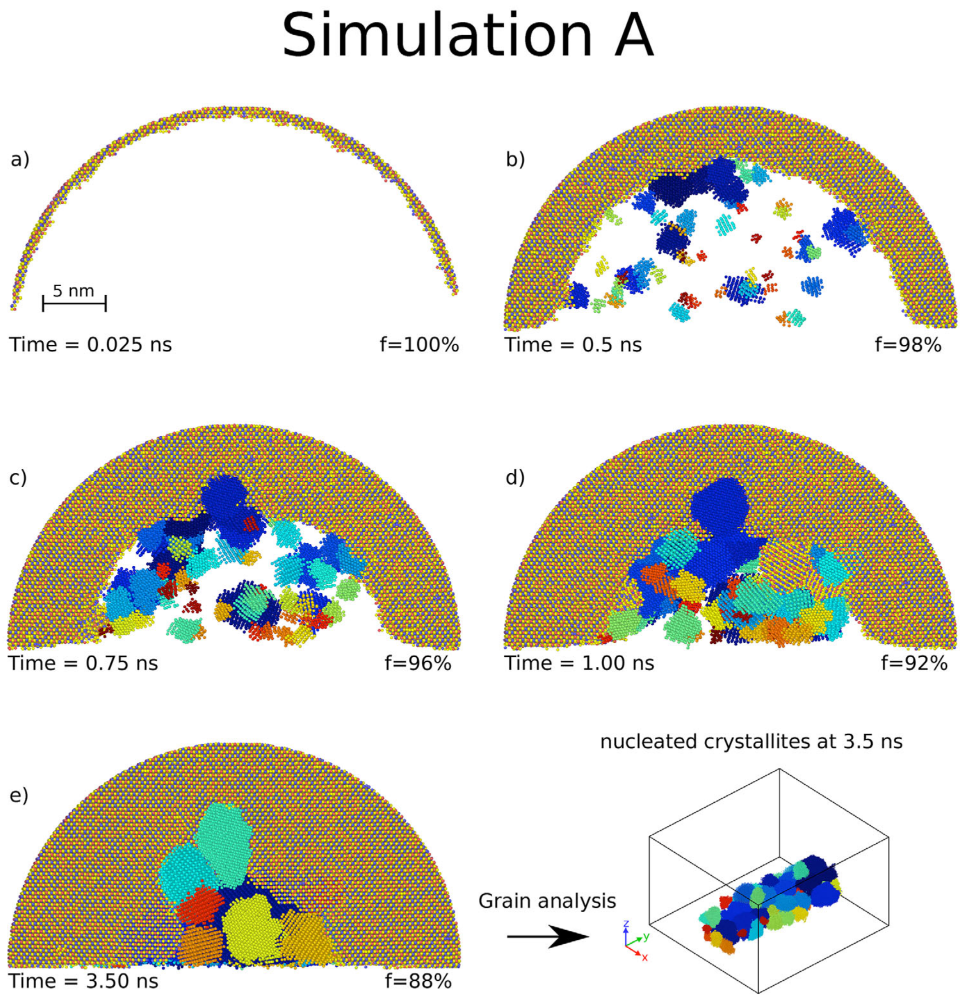

Figure 3. a–e) Snapshots of the recrystallization of the amorphous region at different times (in ns) with the dome thermostatted at 600 K (simulation A). Only recrystallized atoms that were originally present in the amorphous semi-cylindrical dome in Figure 1b,c are shown. Atoms belonging to the largest crystallite growing form the outer amorphous-crystal interface are shown with the same colors of Figure 1c. At the end of the simulation, the largest crystallite contains 541 233 atoms. The smaller crystallites nucleated inside the dome are shown each one in a different color. The fraction of crystallized atoms (number f) belonging to the outer crystallite growing from the rim is given in each panel. A side view of the smaller crystallites (grains) embedded in the largest one is shown on bottom right. These nucleated crystallites touch the confining walls on both sides along y (see Figure 1b).

spherical shape from $v_g = dR(t)/dt$ where the radius R is given by $R = \left(3N/4\pi\rho_{cubic}\right)^{\frac{1}{3}}$.

The evolution of $R_c(t)$ as a function of time in simulation A is reported in Figure S1 (Supporting Information), along with the radius $R(t)$ of the six largest crystallites with a number of atoms greater than 5000 (see Figure 2b). The assumption of a spherical shape for the estimate of the crystal growth velocity in GST is a good approximation for nuclei of the size reported here, as we have shown in a recent work[51] in which we have compared this scheme with the more general method introduced in Ref. [17] that does not make use of any assumption on the shape of crystallites. For the crystallite growing from the rim, the resulting v_g of 7.1 m/s is very close to the value obtained for the growth at 600 K of a crystalline slab in contact with the liquid (heterogeneous crystallization) in our previous work (see Figure 6a in Ref. [32]) while for the six largest crystallites nucleated inside the dome the average v_g of 2.85 ± 0.4 m/s (see Figure S1, Supporting Information) is slightly lower than the values reported for homogeneous crystallization in Ref. [32]. The experimental crystal growth velocity at 600 K is 2.4 m/s as inferred from differential scanning calorimetry and under the assumption that crystallization is due to the growth of preformed spherical nuclei.[52] The overall crystallization time of a few ns of our model is also consistent with the width of set pulses of about 8–9 ns in cell with diameter of 50 nm of Ref. [53]. The lower crystal growth velocity of the nuclei with respect to the growth from the crystal-amorphous rim is due to a geometric factor (the density of adsorption sites as a function of the number of atoms in the nuclei) which depends on the curvature of the growing surface. The contribution from the interface energy term is instead negligible for the size of nuclei considered here and at 600 K. We have addressed this latter issue in a previous work.[51] Anyway, it is not possible to compute v_g from larger nuclei than those considered here (see Figure S1, Supporting

Information) because for longer times the nuclei start to interact with each other. This interaction leads to a reduction of v_g with time (nucleus size), and not to the expected increase due to the change in the geometric factor and to the lower impact of the interface energy term.

We remark that the competition between nucleation and growth from the rim is dependent on temperature because the nucleation rate decreases very rapidly above 600 K.[32] The latent heat released mostly in the outer crystallite growing from the rim is expected to raise the temperature inside the dome and then to reduce the nucleation rate. In simulation A described above, we considered the extreme condition in which the latent heat is removed locally by the thermostat on all ions. Indeed, in the more realistic simulation B in which the latent heat is removed only by a thermostat in the upper part of the model, mimicking the top electrode, we observed an increase of temperature inside the dome during the crystallization process and then the nucleation of a lower number of crystallites. The evolution in time of the fraction of the recrystallized atoms and distribution of the size of the crystallites are shown in Figure 2. We observed nucleation inside the dome of 6 and about 55 crystallites in simulation B and A, respectively. As a consequence, the size of the nuclei is larger in simulation B than in simulation A. The equivalent of Figure 3 for simulation B and a 2D map of the temperature for different simulation times are given in Figures S2 and S3 (Supporting Information). The fraction of the recrystallized atoms from the rim is 94 % of the total number of recrystallized atoms at the end of simulation B. The crystal growth velocity from the rim is 8.4 m/s, while v_g of the nuclei is 3 ± 0.3 m/s. The crystal growth velocities are higher than in simulation A, because the temperature is higher in simulation B both at the rim and inside the dome, due to the latent heat that is removed more slowly and in a more realistic manner from the active region. The evolution in time of $R_c(t)$ (rim) and, as an example, of the radius $R(t)$ of a single nucleus in simulation B is reported in Figure S4 (Supporting Information). Although the crystallization time and the fraction of recrystallized atoms from the rim are overall qualitatively similar in simulations A and B, there are some important differences which suggest that the latent heat of crystallization cannot be completely neglected as occurs in some numerical electrothermal models.[11,12]

Finally, we discuss the more realistic simulation C with the hot spot inside the dome and a second thermostat in the upper part of the model. For simulation C, we report in **Figure 4** the snapshots equivalent to those in Figure 3 for simulation A. The number of crystallites nucleated inside the dome is about 20, which is lower than in simulation A and larger than in simulation B. The evolution in time of the fraction of the recrystallized atoms and distribution of the size of the crystallites are shown in Figure 2.

The 2D map of the temperature for different times in simulation C is shown in **Figure 5**; the temperature is mediated in the y direction (see Figure 1b) in a slice 48 nm thick at the center of the model. The temperature close the confining walls is higher than at the center of the model because the walls have an infinite thermal boundary resistance (the atoms are frozen). This effect is more evident in simulation C, because of the presence of the hot spot inside the dome. The crystal growth velocity from the rim in simulation C is 5.1 m/s, while v_g of the nuclei is 4 ± 0.6 m/s. The difference with the results of simulations A and B (see above) is due to a different temperature field that is lower at the rim and higher in the inner part of the dome where the nuclei appear. The evolution in time of $R_c(t)$ (rim) and, as an example, of the radius $R(t)$ of a single nucleus in simulation C is reported in Figure S4 in the Supporting Information.

Also in the more realistic simulation C, crystallization occurs mainly by growth at the rim, the atoms in the crystallites nucleated inside the dome amount to about 12.5 % of the total number of recrystallized atoms. The predominance of the crystallization from the interface is in agreement with the experimental work of Ref. [54] in which the crystal growth velocities were extracted from electrical measurements in a mushroom memory device under the assumption of a growth-dominated crystallization. The experimental value of the crystal growth velocity of Ref. [54] cannot be directly compared with our results because the measurements refer to a GST material doped to increase the stability of the amorphous phase and the endurance of the device. A similar competition between growth and nucleation has been reported in a recent preprint in which a different machine-learned potential was used to simulate the recrystallization of an amorphous dome of $Ge_1Sb_2Te_4$ in a 794 808-atom cell with temperature conditions corresponding to our simulation A (uniform temperature of 600 K).[55] In this work, for a semi-cylindrical dome 5 nm thick and with a radius of 25 nm, the fraction of atoms recrystallized from the rim is only about 54 % of the total number of recrystallized atoms. This result seems at odds with our findings in the similar simulation A and in the more realistic simulations B and C, but is also in disagreement with the experimental data of Ref. [54], which, however, all refer to a different alloy composition than that used in the simulation of Ref. [55]. As a general comment to conclude this section, we remark that to minimize the cell-to-cell variability in the device it would be desirable to reduce the number and size of the crystallites nucleated within the dome, as the recrystallization just from the crystal/amorphous rim would lead to a more homogenous set state. Our simulations suggest that this would be possible by raising the temperature of the hot spot in the heater and by increasing the thermal boundary resistance with the confining walls made of dielectrics. The ability to control the heterogeneities in the recrystallized material and to reduce grain boundaries is of particular relevance also for the application of phase change materials in artificial synapsis and memristors devices.[56]

2.3. Point Defects in the Recrystallized Material

The recrystallized system provides a very large model of the disordered cubic phase of GST grown at the realistic time scale of the operation of the device. This model allows us to investigate the distribution of point defects, namely antisite defects (cation-anion exchange), vacancies, and vacancy clusters on both sublattices. These defects are of relevance for the electrical conductivity of the cubic crystalline phase. It was shown that clusters of vacancies on the cationic sublattice give rise to localized states at the Fermi level,[57] while antisite defects are responsible for the formation of empty states close to the edge of the conduction band[18,58] (see also Ref. [59] for a review). We remark that in an ideal crystalline cubic GST with the rocksalt

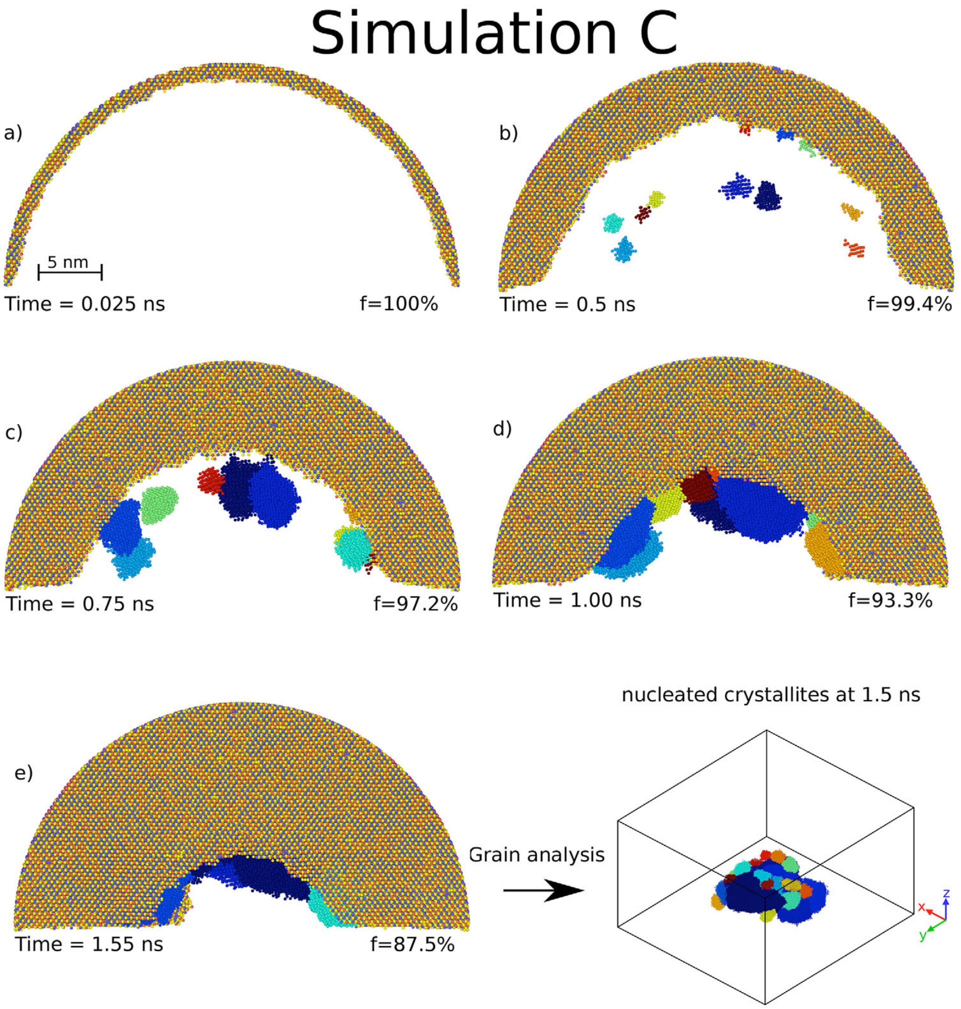

Figure 4. a–e) Snapshots of the recrystallization of the amorphous region at different times (in ns) with a thermostat in contact with the upper electrode and the hot spot inside the dome (simulation C). Only recrystallized atoms that were originally present in the amorphous semi-cylindrical dome in Figure 1b–d are shown. Atoms belonging to the largest crystallite growing form the outer amorphous-crystal interface are shown with the same colors of Figure 1d. The largest crystallite contains 554 752 atoms. The smaller crystallites nucleated inside the dome are shown each one in a different color. The fraction of crystallized atoms (number f) belonging to the outer crystallite growing from the rim is given in each panel. A side view of the smaller crystallites (grains) embedded in the largest one is shown on bottom right. The crystallites nucleated far from the confining walls (see text) lead to the formation of a polycrystalline region at the center of the model.

geometry, the face-centered-cubic (fcc) anionic sublattice if fully occupied by Te, while the fcc cationic sublattice is randomly occupied by 40 % of Ge and Sb and by 20 % of stoichiometric vacancies, i.e., $(\square Ge_2Sb_2)_c(Te_5)_a$, where the subscript a/c stands for anionic/cationic sites. We performed the analysis of the defects in the larger crystallite grown from the rim in simulation A that contains 541 233 atoms.

The largest crystallite is slightly Te-poor with a composition $Ge_{2.021}Sb_{2.03}Te_5$ which amounts to $N_{Ge} = 120\,617$, $N_{Sb} = 121\,327$ and $N_{Te} = 299\,288$ total number of Ge, Sb and Te atoms. The missing Te atoms enrich the amorphous regions between the crystalline grains. This composition arises, however, also from the presence of vacancies on both the cationic and anionic sublattice and of antisites Te_c, Sb_a and Ge_a. The composition of the other six largest crystallites nucleated inside the dome is given in Table S1 (Supporting Information).

To assess the reliability of the NN potential in describing antisite defects, we compared the formation energy of different defects obtained from NN and DFT calculations within the framework used to generate the NN potential itself.[32] We considered the 270-atom supercell of the ideal cubic GST (random occupation of the cation sublattice with Ge/Sb and 20 % of vacancies) generated in Ref. [45]. We then switched a Te atom with a Ge atom (Te_c-Ge_a pair) or with an Sb atom (Te_c-Sb_a pair) or we moved a Te atom in a cationic vacancy ($Te_{\square}$). We considered three different switches for each type of defect. The DFT formation energy is 1.60 ± 0.50 eV for $Te_{\square}$, 1.35 ± 0.10 eV for the Te_c-Ge_a pair, and 1.10 ± 0.10 eV for the Te_c-Sb_a pair. The root-mean-square-error (RMSE) between DFT and NN formation energies is 0.28 eV for $Te_{\square}$, 0.105 eV for the Te_c-Ge_a pair, and 0.085 eV for the Te_c-Sb_a pair. Overall, the RMSE error is lower than the spread in the formation energy due to different environments.

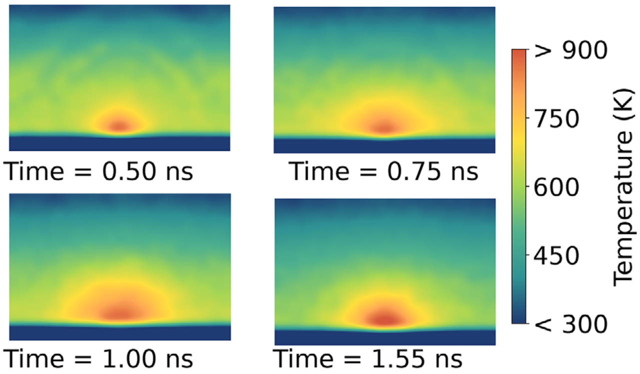

Figure 5. A 2D map of the temperature at different times in simulation C. The *xz* plane (see Figure 1b) was divided into a 240 × 165 grid (39 600 pixels). The atomic temperature was then averaged over each pixel area (2 × 2 Å^2) and along the *y* direction in a slice 48 nm thick at the center of the model, far from the confining walls along *y*. A Gaussian filtering was then used to smear out the fluctuations.

We then identified the antisite defects in the crystallites from the analysis of the partial coordination numbers (*NC*s).

For example, a Te atom on the anionic sublattice should have $NC_{\mathrm{TeTe}} = 0$, while $NC_{\mathrm{TeTe}} \neq 0$ for an antisite Te atom. Therefore, we label a Te atom with $NC_{\mathrm{TeTe}} \geqslant 3$ as an antisite atom, by assuming that a cationic site could have at most three vacancies as first neighbors on the anionic sites. Similarly, Ge_a and Sb_a atoms were identified from the condition $NC_{\mathrm{GeGe}}+NC_{\mathrm{GeSb}} \geqslant 3$ or $NC_{\mathrm{SbGe}}+\mathrm{NC}_{\mathrm{SbSb}} \geqslant 3$, again assuming that an anionic site could have at most three vacancies as first neighbors on the cationic sites (see below). We found only 36 Ge_a, but 1606 Sb_a and 3457 Te_c. Therefore, only a fraction of Te_c arises from an exchange with cations, the majority of Te_c consists of Te atoms occupying the stoichiometric cationic vacancies. The Te_c, Sb_a, and Ge_a antisites are overall 1.1, 1.3, 0.03 % of the Te, Sb, and Ge atoms. The number of different antisites in the six largest crystallites nucleated inside the dome is given in Table S2 (Supporting Information).

Then, we estimated the number of vacancies on the cationic and anionic sublattices from the average coordination numbers given in **Table 1**. The distribution of the coordination numbers for anionic and cationic sites is shown in **Figure 6**. The number of cationic vacancies is obtained from the average coordination number of the atoms occupying anionic sublattice $\mathrm{n_a}$ (see Table 1) as $\square_c = (6\text{-}\mathrm{n_a})\mathrm{N_a}/6$ where the factor six comes from the presence of six nearest neighbors and $\mathrm{N_a}$ is the number atoms occupying anionic sublattice (i.e., Ge_a, Sb_a and Te_a). Similarly, the number of anionic vacancies is obtained by $\square_a = (6\text{-}\mathrm{n_c})\mathrm{N_c}/6$. This calculation yields the following composition including antisites and vacancies on the two sublattices $(\square_{0.9173}\mathrm{Ge}_{2.0155}\mathrm{Sb}_{2.0012}\mathrm{Te}_{0.0578})_c(\square_{0.0277}\mathrm{Ge}_{0.0006}\mathrm{Sb}_{0.0268}\mathrm{Te}_{4.9449})_a$ to be compared with the $(\square\mathrm{Ge}_2\mathrm{Sb}_2)_c(\mathrm{Te}_5)_a$ formula unit for the ideal crystal with stoichiometric vacancies only.

Table 1. Average coordination numbers for each chemical species in the largest crystallite of recrystallized GST. $\mathrm{n_c}$ and $\mathrm{n_a}$ indicate the average coordination number of atoms on the cationic and anionic sublattice. The coordination in the ideal stoichiometric compound is given in parenthesis.

	$\mathrm{n_{Ge}}$	$\mathrm{n_{Sb}}$	$\mathrm{n_{Te}}$	$\mathrm{n_c}$	$\mathrm{n_a}$
Coordination	5.97 (6.0)	5.96 (6.0)	4.93 (4.8)	5.97 (6.0)	4.90 (4.8)

About 10 % (0.91 vs 1.0) of the stoichiometric vacancies on the cationic sublattice is filled by Ge, Sb and Te antisite (Te_c). A fraction of about 0.5 % of the anionic sublattice is also occupied by vacancies.

The overall concentration of antisites is below 0.95 % which means that the two sublattices are very strongly chemically ordered in a crystallite grown in a few ns at 600 K. This is at odds with the recent finding of a strong chemical disorder during the growth of the metastable cubic phase of the $\mathrm{Sb_2Te_3}$ which is a parent compound[60] of $\mathrm{Ge_2Sb_2Te_5}$ that can in fact be seen as a pseudobinary alloy along the GeTe-$\mathrm{Sb_2Te_3}$ tie-line in the ternary phase diagram.

We then went a step further by analyzing the clustering of vacancies and antisites. The clustering of vacancies in the cationic sublattice can be inferred from the distribution of the coordination numbers of atoms occupying anionic sublattice (mostly Te) as shown in Figure 6. Most of these atoms are 5-coordinated which means that they have a single nearest neighbor vacancy, while about than 20 % of Te atoms have two nearest neighbor vacancies (fourfold coordinated), and about 5 % have three nearest neighbor vacancies (threefold coordinated), and only 0.4% of Te atoms are twofold coordinated. Regarding the clustering of antisites, we consider two antisites belonging to the same cluster if their distance is shorter than the next nearest neighbor distance on the fcc sublattice (6.1 Å).

The distribution of the size of the clusters of antisites is shown in **Figure 7**. Overall, 71 % of the antisites are isolated, while 1455 out of 5099 antisites are arranged in clusters of different sizes.

About 3% of these clusters has a swapped pair of adjacent atoms (Ge_a/Sb_a-Te_c first neighbors), while most of the clusters with two/three antisite atoms are either linear chains of Te atoms or defective four-membered rings, such as isolated AAAA or BBBB rings where A = Ge/Sb and B = Te, or a pair of AAAB/BBBA rings forming a cube. Snapshots of the different types of antisite clusters are shown in **Figure 8**. Overall, we observed a rather large fraction of antisite defects (0.95 % of the total number of atoms) which mostly form chains of Te-Te

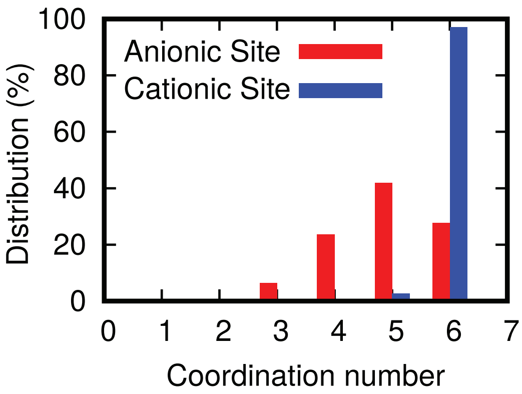

Figure 6. Distribution of the coordination number for atoms in the anionic (red) and cationic (blue) sites of the large crystallite grown from the rim (541 231 atoms) in simulation A.

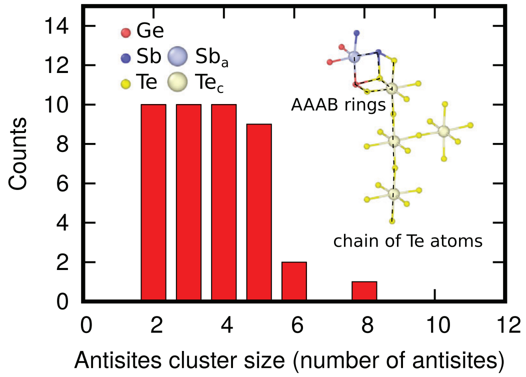

Figure 7. Number of clusters of antisites with different sizes. A snapshot of a 5-membered cluster is given in the inset which is made of a pair of AAAB/BBBA rings and a long chain of Te atoms.

homopolar bonds. According to the DFT calculations in Ref. [18, 58], these defects give rise to localized states close to the conduction band edge. Moreover, a sizable fraction of Te atoms (5 %) are threefold coordinated due to the clustering of three vacancies on the cationic sublattice. These latter configurations are responsible for localized states at the edge of the valence band as shown by DFT calculations in Ref. [18, 57].

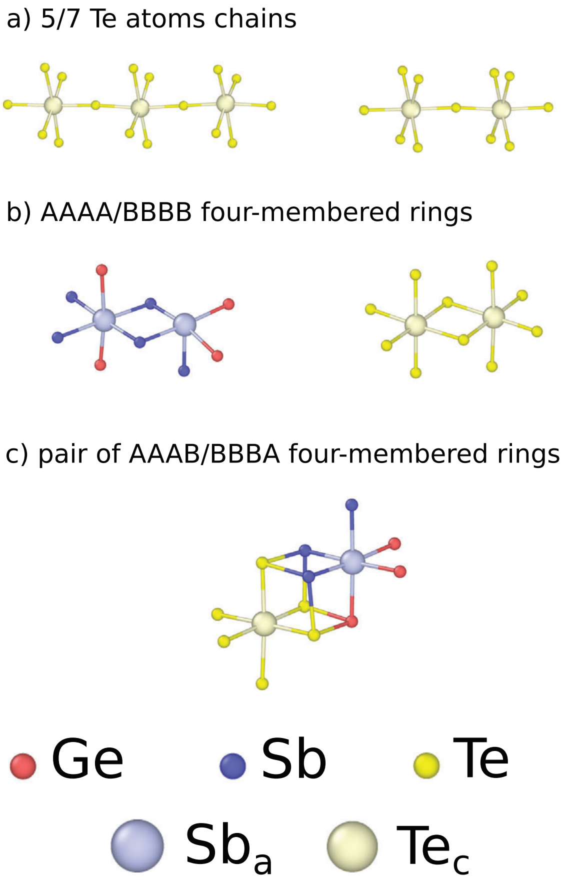

Figure 8. Snapshots of the different types of clusters of antisites.

3. Conclusion

In summary, we have shown that the NN potential developed with the DeepMD code allows simulating the crystallization process of the prototypical phase change compound $Ge_2Sb_2Te_5$ at the length and time scales of the real memory devices. This first multimillion atom simulation of a model mimicking the real memory device in the Wall architecture, unveils the subtle competition between homogeneous crystal nucleation and crystal growth from the crystal/amorphous rim and its dependence on the temperature profile generated by the programming protocol. The simulations provided a vivid atomistic picture of unprecedented realism of the operation of the memory device and they pave the way to the simulation of more complex transformation at the device scale such as the crystallization and phase separation in Ge-rich GeSbTe alloys exploited in embedded memories[4,5] and whose kinetics details are still largely unknown. Moreover, the recrystallized system provided a very large model of cubic GST grown at the real time scale of the memory operation which allowed us to gain a statistically sound distribution of the defects (antisites and vacancies) that are known to give rise to the localized states in the band gap which control the electrical resistivity of the set state.

4. Computational Details

MD simulations have been performed using the NN potential of Ref. [32], generated with the DeePMD package[37–39] by fitting a database DFT energies and forces of around 180,000 configurations of small supercells (57-108 atoms). The Perdew–Burke–Ernzerhof (PBE)[61] exchange and correlation functional and norm conserving pseudopotentials were used.[62,63] The potential was validated in Ref. [32] on the structural and dynamical properties of the liquid, amorphous and crystalline phases and it was then exploited to study the crystallization kinetics in the bulk with supercells containing up to 12 900 atoms. The LAMMPS code[64] has been used as MD driver with a time step of 2 fs and a Nosé-Hoover thermostat.[65,66] We note that a 3 ns simulation of our 2.795 million-atom model requires about 10 000 gpu-hours of Nvidia Ampere 100 gpu on the Leonardo-booster machine at Cineca (Bologna, Italy). The reliability of the PBE-DFT framework in reproducing experimental data has been assessed on several properties of GST, including the structural properties of the amorphous phase (see Ref. [67] for a comprehensive comparison with experiments and DFT results with other functionals), vibrational properties and thermal transport of the amorphous and crystalline phase[68–71] and crystal growth velocity in the supercooled liquid,[51] just to name a few relevant for the present work.

Supporting Information

Supporting Information is available from the Wiley Online Library or from the author.

Acknowledgements

The authors equally contributed to the work. The project received funding from European Union NextGenerationEU through the Italian Ministry of University and Research under PNRR M4C2I1.4 ICSC Centro Nazionale di

Ricerca in High Performance Computing, Big Data and Quantum Computing (Grant No. CN00000013). The authors thank Matteo Baldo, Elisa Petroni and Sergio Piva for the helpful discussions.

Conflict of Interest

The authors declare no conflict of interest.

Data Availability Statement

Initial and final configurations of the three simulations A/B/C and a movie of the crystallization process in simulation C are available as additional material in the Materials Cloud repository at https://doi.org/10.24435/materialscloud:4f-wv. Complete trajectories of the crystallization process for the three simulations A/B/C are available upon request.

Keywords

crystallization, electronic memories, machine learning potentials, neural networks, phase change materials

Received: February 11, 2025
Revised: April 4, 2025
Published online: June 9, 2025

---

[1] M. Wuttig, N. Yamada, *Nat. Mater.* **2007**, *6*, 824.
[2] P. Noé, C. Vallée, F. Hippert, F. Fillot, J.-Y. Raty, *Semicond. Sci. Technol.* **2017**, *33*, 013002.
[3] P. Fantini, *J. Phys. D: Appl. Phys.* **2020**, *53*, 283002.
[4] P. Cappelletti, R. Annunziata, F. Arnaud, F. Disegni, A. Maurelli, P. Zuliani, *J. Phys. D* **2020**, *53*, 193002.
[5] A. Redaelli, E. Petroni, R. Annunziata, *Mater. Sci. Semicond. Process.* **2022**, *137*, 106184.
[6] D. Kuzum, R. G. Jeyasingh, B. Lee, H.-S. P. Wong, *Nano Lett.* **2012**, *12*, 2179.
[7] T. Tuma, A. Pantazi, M. Le Gallo, A. Sebastian, E. Eleftheriou, *Nat. Nanotechnol.* **2016**, *11*, 693.
[8] A. Sebastian, M. Le Gallo, R. Khaddam-Aljameh, E. Eleftheriou, *Nat. Nanotechnol.* **2020**, *15*, 529.
[9] W. Zhang, R. Mazzarello, M. Wuttig, E. Ma, *Nat. Rev. Mater.* **2019**, *4*, 150.
[10] M. Salinga, E. Carria, A. Kaldenbach, M. Bornhofft, J. Benke, J. Mayer, M. Wuttig, *Nat. Commun.* **2013**, *4*, 2371.
[11] A. Redaelli, A. Pirovano, A. Benvenuti, A. L. Lacaita, *J. Appl. Phys.* **2008**, *103*, 111101.
[12] (Ed.: A. Redalli), *Phase Change Memory: Device Physics, Reliability and Applications*, Spinger International Publishing, **2020**.
[13] J. Hegedüs, S. Elliott, *Nat. Mater.* **2008**, *7*, 399.
[14] T. H. Lee, S. R. Elliott, *Phys. Rev. Lett.* **2011**, *107*, 145702.
[15] J. Kalikka, J. Akola, R. Jones, *Phys. Rev. B* **2016**, *94*, 134105.
[16] I. Ronneberger, W. Zhang, H. Eshet, R. Mazzarello, *Adv. Funct. Mater.* **2015**, *25*, 6407.
[17] I. Ronneberger, W. Zhang, R. Mazzarello, *MRS Commun.* **2018**, *8*, 1018.
[18] Y. Xu, Y. Zhou, X.-D. Wang, W. Zhang, E. Ma, V. L. Deringer, R. Mazzarello, *Adv. Mater.* **2022**, *34*, 2109139.
[19] F. Rao, K. Ding, Y. Zhou, Y. Zheng, M. Xia, S. Lv, Z. Song, S. Feng, I. Ronneberger, R. Mazzarello, W. Zhang, E. Ma, *Science* **2017**, *358*, 1423.
[20] T. H. Lee, S. R. Elliott, *Adv. Mater.* **2017**, *29*, 1700814.
[21] J. Behler, M. Parrinello, *Phys. Rev. Lett.* **2007**, *98*, 146401.
[22] A. P. Bartók, M. C. Payne, R. Kondor, G. Csányi, *Phys. Rev. Lett.* **2010**, *104*, 136403.
[23] G. C. Sosso, G. Miceli, S. Caravati, J. Behler, M. Bernasconi, *Phys. Rev. B* **2012**, *85*, 174103.
[24] G. C. Sosso, G. Miceli, S. Caravati, F. Giberti, J. Behler, M. Bernasconi, *J. Phys. Chem. Lett.* **2013**, *4*, 4241.
[25] G. C. Sosso, M. Salvalaglio, J. Behler, M. Bernasconi, M. Parrinello, *J. Phys. Chem. C* **2015**, *119*, 6428.
[26] F. C. Mocanu, K. Konstantinou, T. H. Lee, N. Bernstein, V. L. Deringer, G. Csányi, S. R. Elliott, *J. Phys. Chem. B* **2018**, *122*, 8998.
[27] D. Dragoni, J. Behler, M. Bernasconi, *Nanoscale* **2021**, *13*, 16146.
[28] D. Lee, K. Lee, D. Yoo, W. Jeong, S. Han, *Comput. Mater. Sci.* **2020**, *181*, 109725.
[29] Y. Zhou, W. Zhang, E. Ma, V. L. Deringer, *Nat. Electr.* **2023**, *6*, 746.
[30] G. Wang, Y. Sun, J. Zhou, Z. Sun, *J. Phys. Chem. C* **2023**, *127*, 24724.
[31] W. Yu, Z. Zhang, X. Wan, J. Su, Q. Gui, H. Guo, H.-x. Zhong, J. Robertson, Y. Guo, *Chem. Mater.* **2023**, *35*, 6651.
[32] O. Abou El Kheir, L. Bonati, M. Parrinello, M. Bernasconi, *npj Comput. Mater.* **2024**, *10*, 33.
[33] B.-Q. Wang, T.-Y. Zhao, H.-R. Ding, Y.-T. Liu, N.-K. Chen, M. Niu, X.-D. Li, M. Xu, H.-B. Sun, S. Zhang, X.-B. Li, *Acta Mater.* **2024**, *276*, 120123.
[34] D. Baratella, O. Abou El Kheir, M. Bernasconi, *Acta Mater.* **2025**, *284*, 120608.
[35] O. R. Dunton, T. Arbaugh, F. W. Starr, *J. Chem. Phys.* **2025**, *162*, 034501.
[36] S. Gabardi, E. Baldi, E. Bosoni, D. Campi, S. Caravati, G. Sosso, J. Behler, M. Bernasconi, *J. Phys. Chem. C* **2017**, *121*, 23827.
[37] H. Wang, L. Zhang, J. Han, W. E, *Comput. Phys. Commun.* **2018**, *228*, 178.
[38] L. Zhang, J. Han, H. Wang, R. Car, W. E, *Phys. Rev. Lett.* **2018**, *120*, 143001.
[39] D. Lu, H. Wang, M. Chen, L. Lin, R. Car, W. E, W. Jia, L. Zhang, *Comput. Phys. Commun.* **2021**, *259*, 107624.
[40] F. Arnaud, P. Ferreira, F. Piazza, A. Gandolfo, P. Zuliani, P. Mattavelli, E. Gomiero, G. Samanni, J. Jasse, C. Jahan, J. P. Reynard, R. Berthelon, O. Weber, A. Villaret, B. Dumont, J. C. Grenier, R. Ranica, C. Gallon, C. Boccaccio, A. Souhaite, L. Desvoivres, D. Ristoiu, L. Favennec, V. Caubet, S. Delmedico, N. Cherault, R. Beneyton, S. Chouteau, P. O. Sassoulas, L. Clement, et al., in *2020 IEEE International Electron Devices Meeting (IEDM)*, **2020**, pp. 24.2.1–24.2.4.
[41] L. Laurin, M. Baldo, E. Petroni, G. Samanni, L. Turconi, A. Motta, M. Borghi, A. Serafini, D. Codegoni, M. Scuderi, S. Ran, A. Claverie, D. Ielmini, R. Annunziata, A. Redaelli, in *2023 IEEE International Reliability Physics Symposium (IRPS)*, **2023**, pp. 1–7.
[42] R. Ranica, R. Berthelon, A. Gandolfo, G. Samanni, E. Gomiero, J. Jasse, P. Mattavelli, J. Sandrini, M. Querre, Y. Le-Friec, J. Poulet, V. Caubet, L. Favennec, C. Boccaccio, G. Ghezzi, C. Gallon, J. C. Grenier, B. Dumont, O. Weber, A. Villaret, R. Beneyton, N. Cherault, D. Ristoiu, S. Del Medico, O. Kermarrec, J. P. Reynard, P. Boivin, A. Souhaite, L. Desvoivres, S. Chouteau, et al., in *2021 IEEE International Electron Devices Meeting (IEDM)*, IEEE, **2021**, pp. 28–1.
[43] M. Boniardi, A. Redaelli, C. Cupeta, F. Pellizzer, L. Crespi, G. D'Arrigo, A. L. Lacaita, G. Servalli, in *2014 IEEE International Electron Devices Meeting*, **2014**, pp. 29.1.1–29.1.4.
[44] A. Stukowski, *Modelling Simul. Mater. Sci. Eng.* **2010**, *18*, 1.
[45] S. Caravati, M. Bernasconi, T. Kühne, M. Krack, M. Parrinello, *J. Phys. Condens. Matter* **2009**, *21*, 255501.
[46] J. Lee, E. Bozorg-Grayeli, S. Kim, M. Asheghi, H.-S. P. Wong, K. E. Goodson, *Appl. Phys. Lett.* **2013**, *102*, 191911.
[47] M. Cobelli, D. Dragoni, S. Caravati, M. Bernasconi, *Phys. Rev. Mater.* **2021**, *5*, 045004.

[48] D. Baratella, D. Dragoni, M. Bernasconi, *Phys. Status Solidi RRL* **2022**, *16*, 2100470.

[49] M. Baldo, O. Melnic, M. Scuderi, G. Nicotra, M. Borghi, E. Petroni, A. Motta, P. Zuliani, A. Redaelli, D. Ielmini, in *2020 IEEE International Electron Devices Meeting (IEDM)*, **2020**, pp. 13.3.1–13.3.4.

[50] P. J. Steinhardt, D. R. Nelson, M. Ronchetti, *Phys. Rev. B* **1983**, *28*, 784.

[51] D. Acharya, O. A. E. Kheir, S. Marcorini, M. Bernasconi, *Nanoscale* **2025**, https://doi.org/10.1039/d5nr00283d.

[52] J. Orava, A. Greer, B. Gholipour, D. Hewak, C. Smith, *Nat. Mater.* **2012**, *11*, 279.

[53] W. J. Wang, L. P. Shi, R. Zhao, H. K. Lim, K. G. andLee, T. C. Chong, Y. H. Wu, *Appl. Phys. Lett.* **2008**, *93*, 043121.

[54] A. Sebastian, M. Le Gallo, D. Krebs, *Nat. Commun.* **2014**, *5*, 4314.

[55] Y. Zhou, D. F. Thomas du Toit, S. R. Elliott, W. Zhang, V. L. Deringer, *arXiv preprint arXiv:2502.08393* **2025**.

[56] I. Boybat, M. Le Gallo, S. Nandakumar, T. Moraitis, T. Parnell, T. Tuma, B. Rajendran, Y. Leblebici, A. Sebastian, E. Eleftheriou, *Nature communications* **2018**, *9*, 2514.

[57] W. Zhang, A. Thiess, P. Zalden, R. Zeller, P. H. Dederichs, J.-Y. Raty, M. Wuttig, S. Blugel, R. Mazzarello, *Nat. Mater.* **2012**, *11*, 952.

[58] F. C. Konstantinou, K. Mocanu, J. Akola, *Phys. Rev B* **2022**, *106*, 184103.

[59] J.-J. Wang, Y.-Z. Xu, R. Mazzarello, M. Wuttig, W. Zhang, *Materials* **2017**, *10*, 862.

[60] Y. Zheng, W. Song, Z. Song, Y. Zhang, T. Xin, C. Liu, Y. Xue, S. Song, B. Liu, X. Lin, V. G. Kuznetsov, I. I. Tupitsyn, A. V. Kolobov, Y. Cheng, *Adv. Sci.* **2023**, *11*, 2301021.

[61] J. P. Perdew, K. Burke, M. Ernzerhof, *Phys. Rev. Lett.* **1996**, *77*, 3865.

[62] S. Goedecker, M. Teter, J. Hutter, *Phys. Rev. B* **1996**, *54*, 1703.

[63] M. Krack, *Theor. Chem. Acc.* **2005**, *114*, 145.

[64] A. P. Thompson, H. M. Aktulga, R. Berger, D. S. Bolintineanu, W. M. Brown, P. S. Crozier, P. J. in 't Veld, A. Kohlmeyer, S. G. Moore, T. D. Nguyen, R. Shan, M. J. Stevens, J. Tranchida, C. Trott, S. J. Plimpton, *Comp. Phys. Comm.* **2022**, *271*, 108171.

[65] S. Nosé, *J. Chem. Phys.* **1984**, *8*, 511.

[66] W. J. Hoover, *Phys. Rev. A* **1985**, *31*, 1695.

[67] I. Pethes, A. Piarristeguy, A. Pradel, J. Michalik, S. Darpentigny, A. Zitolo, R. Escalier, P. Jvri, *J. Amer. Ceramic Soc.* **2025**, *108*, e20258.

[68] D. Campi, L. Paulatto, G. Fugallo, F. Mauri, M. Bernasconi, *Phys. Rev. B* **2017**, *95*, 024311.

[69] G. C. Sosso, S. Caravati, R. Mazzarello, M. Bernasconi, *Phys. Rev. B* **2011**, *83*, 134201.

[70] G. Sosso, S. Caravati, C. Gatti, S. Assoni, M. Bernasconi, *J. Phys. Condens. Matter* **2009**, *21*, 245401.

[71] L. Yang, B.-Y. Cao, *J. Phys. D: Appl. Phys.* **2021**, *54*, 505302.